Journal of
MATERIALS RESEARCH

Quantitative analysis of microstructures produced by creep of Ti–48Al–2Cr–2Nb–1B: Thermal and athermal mechanisms

M. A. Morris and M. Leboeuf
Institute of Structural Metallurgy, University of Neuchâtel, Av. Bellevaux, 51, 2000 Neuchâtel, Switzerland

(Received 14 February 1997; accepted 5 June 1997)

A γ-based TiAl alloy with equiaxed microstructure and fine grain size has been studied to analyze the deformation mechanisms responsible for the creep behavior. The microstructures produced by creep and high temperature deformation have been examined by TEM to obtain information about the different aspects characterizing the primary and secondary stages of creep. Mechanical twinning has been confirmed to occur in a fraction of the grains that never exceeds 50% while $1/2\langle 110\rangle$ dislocations are active within all the γ grains. The twins are only responsible for a small amount of strain, but they lead to a subdivision of the microstructure and determine (directly or indirectly) the hardening process observed during the primary stage of creep. We have proposed that during the secondary stage the creep rate is determined by the unblocking of pinned dislocations by processes such as a pipe diffusion or cross slip that allow thermally activated glide of $1/2\langle 110\rangle$ dislocations on (001) planes.

I. INTRODUCTION

Titanium aluminides based on the two-phase ($\gamma + \alpha_2$) microstructure are very attractive for intermediate temperature (600–850 °C) aerospace applications because of their excellent high temperature strength, low density, and good oxidation resistance.[1,2] Considerable research effort has been devoted to study the creep deformation of this type of alloy and it has been shown that the creep resistance depends significantly on the microstructure.[3–8] The increase in creep resistance of fully lamellar microstructures is generally attributed to the α_2 laths and γ/γ interfaces acting as barriers to slip.[4,9] On the other hand, it has been suggested that the decreased creep resistance of the duplex microstructure compared to that of the equiaxed γ microstructure is a result of the increased glide mobility of $1/2\langle 110\rangle$ dislocations within the γ matrix[10] of the former. Although it is generally accepted that the alloys exhibit power law creep behavior, the values of the stress exponent, n, appear to increase with increasing applied stress.[9,11] This has been interpreted as being due to a transition from diffusional creep at low stresses to dislocation glide creep at high stresses.[5,12–14]

Although mechanical twinning during creep deformation of TiAl alloys has been extensively reported,[5,15–17] its contribution to the creep process is not easily interpreted since traditional creep theories do not include such contributions. Also it has been suggested that mechanical twinning differs between lamellar structures and equiaxed γ grains.[16]

The present study has been carried out to examine the creep behavior of an alloy of composition Ti–48Al–2Cr–2Nb–1B with equiaxed microstructure and fine grain size. The addition of boron prevented grain growth during high temperature forging carried out to reduce segregation. The aim of the study was to examine the creep resistance of such small grain size material and to relate it to the active mechanisms responsible for the deformation process. In particular, we have examined the influence of mechanical twinning on primary creep compared to that observed in alloys with large grain size previously studied.[17] Also, we have separated the different contributions from glide of $1/2\langle 110\rangle$ dislocations and twinning during the secondary stage of creep.

II. EXPERIMENTAL

The analyzed composition of the alloy used in the present study is Ti–48Al–2Cr–2Nb–1B (at. %). It was received in the as-forged state (carried out at 1150 °C to 70% strain) and its microstructure examined before and after annealing for 1 h at 1250 °C followed by air cool. This treatment produced an equiaxed microstructure characterized by a distribution of small γ grains with the α_2 phase distributed at boundaries and triple junctions.

The creep tests were carried out in tension on cylindrical specimens machined to a diameter of 3 mm and with 28 mm gauge length. Their surfaces were subsequently mechanically polished and electropolished using a solution of 5% perchloric acid in methanol. The creep machine used was equipped with Andrade's type cam with a profile that allowed the stress to be maintained constant throughout the test. Tests were performed at 700 °C for stresses ranging between 260 and 360 MPa. The machine was equipped with a data acquisition

unit which monitored the elongation of the specimens every second. The temperature of the specimens was maintained constant with a precision of ±0.2 °C and their elongation was monitored with a precision of about ±2 μm. At the end of the creep tests, the specimens were rapidly cooled under load to avoid any dislocation rearrangement prior to microstructural observations. Also some tests were performed under stresses of 260 and 340 MPa to determine the activation energy of the creep process at constant structure by carrying out fast temperature jumps every 15 °C between 675 and 720 °C. Between these jumps the structure was allowed to stabilize before the next jump was performed in each case, ensuing that the new strain rate measured was characteristic of the controlling mechanism at the new temperature.

Microstructural analysis of the undeformed and deformed specimens was performed by x-ray diffraction, transmission electron microscopy (TEM), and scanning electron microscopy (SEM). The latter was carried out using crystallographic contrast from backscattered electrons to obtain information about any large scale substructure formation during the primary stage of creep. Quantitative measurements of the grain size, volume fraction of the α_2 phase, as well as other aspects of the deformed structures were carried out using an image analyzer directly attached to the SEM which allowed accumulation of a large number of images. At least 300 grains were used for each measured condition.

For all TEM and SEM observations disks were cut perpendicular to the tensile axis from the deformed samples (i.e., the normal directions of the disks were parallel to the tensile axis) and electropolished. The electropolished samples were prepared by standard jet polishing techniques using a solution of 5% perchloric acid, 30% butan-1-ol and 65% methanol at −20 °C and 50 mA, but only the TEM samples were polished to produce a hole. Dislocation analysis was carried out from projected images obtained by tilting the specimens to different known orientations (zone axes) from which different diffraction vectors were chosen to obtain invisibility under some contrast conditions. Weak beam images were taken using the g: 3g condition.

III. RESULTS

Figure 1(a) shows an example of the initial equiaxed microstructure of the annealed alloy obtained by atomic number contrast using backscattered electrons in the SEM. Quantitative measurements confirmed that the average size of the equiaxed γ grains was about 12 ± 2 μm and the volume fraction of α_2 phase (seen as brighter regions distributed along grain boundaries) was about 13%. Also present were large (about 1–5 μm in size) TiB_2 particles which were also analyzed by x-ray

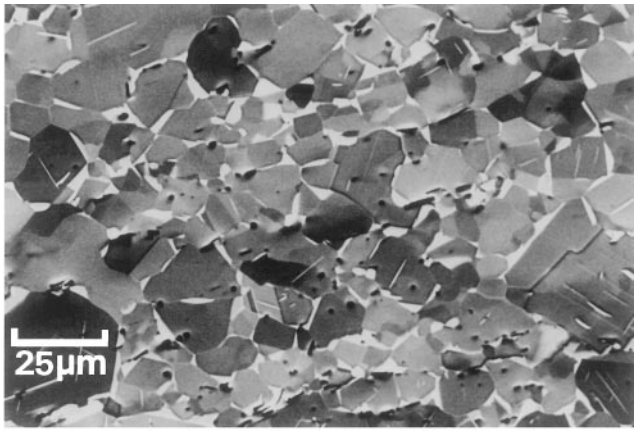

(a)

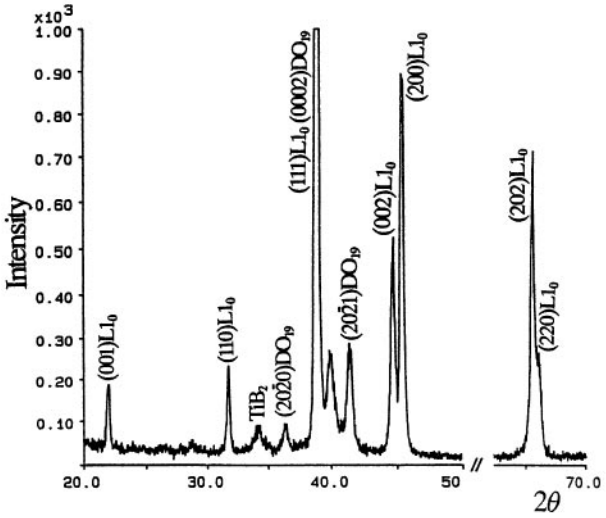

(b)

FIG. 1. (a) Typical example of the initial equiaxed microstructure obtained by annealing at 1250 °C. The bright regions correspond to the α_2 phase. (b) X-ray spectrum obtained from the annealed material shown in (a).

diffraction as illustrated in the spectrum of Fig. 1(b). From the latter (as well as from the x-ray spectra obtained for any annealed condition) we confirmed, by comparing the relative peak heights of the alloy with those from powder samples, that there was no preferred orientation or specific texture in the material. Although the forged material contained a high density of defects, both in terms of low angle boundaries and individual dislocations, the annealed alloy that was used for creep and tensile tests was initially dislocation-free, with only some isolated grains still containing low angle boundaries.

The strain-time curves obtained from the tensile creep tests are shown in Fig. 2 together with curves showing the variation of strain rate as a function of strain. From the latter we confirmed that the initial instantaneous strains obtained on loading are not sensitive

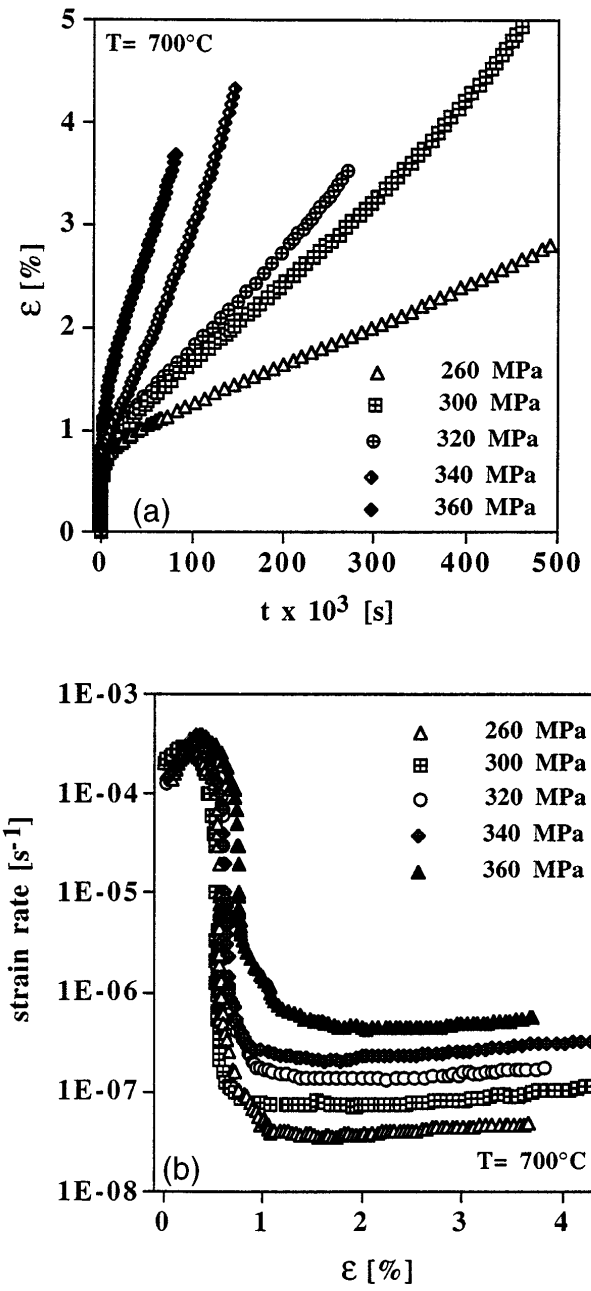

FIG. 2. (a) Typical strain-time curves and (b) corresponding strain rate variation as a function of strain obtained from the creep tests carried out under different applied stresses.

to applied stress, ranging between 0.4 and 0.6% for the two extreme stresses of 260 and 360 MPa used in the present study. Also the initial strain rates ranged between 2 and 4×10^{-4} s^{-1} and decreased rapidly during the first 1% strain. Generally the strain rate reached minimum values at about 1.5–2% strain, and ranging between 3×10^{-8} and 4.5×10^{-7} s^{-1} for the lower and higher stresses used. Thereafter the strain rate remained rather constant to about 3% strain and slowly accelerated after 3–3.5% strain. Most tests were performed to about 4–5% strain. Other tests were interrupted at intermediate strains between 0.8 and 3% to analyze the evolution of the deformed microstructures. From temperature jumps carried out during the secondary stage of creep (between 1.5 and 2.6% strain), we have measured an activation energy of 430 kJ/mol independent of the applied stresses used for the tests.

In parallel, tensile tests were also performed at 700 °C under constant strain rate control mode using strain rates ranging between 3×10^{-4} and 4×10^{-6} s^{-1}. From these tests we remeasured the values of flow stress at 0.2% strain, the maximum flow strength and the tensile ductility, given in Table I. Also from these tests the work hardening rates were measured as a function of strain and the values are shown in Fig. 3. The hardening rate decreases steadily with strain and is ten times higher at about 0.2% strain than at about 3% deformation. The tensile ductility of the samples varied between 2 and 6% for the higher and lower strain rates used, respectively.

Finally additional tensile tests were performed at 700 °C using strain rate jumps over a wide range of strain. From these tests we have determined the activation volume, V, characterizing the mechanism con-

TABLE I. Data from tensile tests (strain rate controlled).

Strain rate (s^{-1})	$\sigma_{0.2}$ (MPa)	σ_{max} (MPa)	ϵ (%)
3×10^{-4}	398	530	1.93
3×10^{-5}	360	503	1.53
1×10^{-5}	347	433	2.3
4×10^{-6}	335	456	6.1

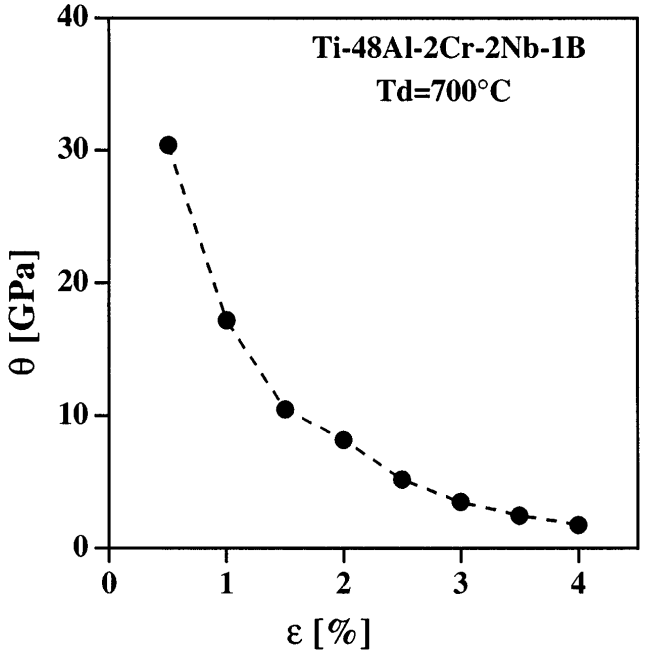

FIG. 3. Plot of strain hardening versus strain measured from the tensile test carried out at constant strain rate 4×10^{-6} s^{-1}.

trolling the deformation process as given by $V = mkT(\Delta \ln \dot{\epsilon}/\Delta\sigma)$, where $m = 3$ is the Taylor factor, k the Boltzmann constant, T the absolute temperature, $\dot{\epsilon}$ the strain rate, and σ the corresponding stress. The value measured, $V = (7.5 \pm 0.5) \times 10^{-27}$ m^3, was confirmed to be strain independent. Such a value corresponds to about $V = 330 \pm 25b^3$, where $b = 2.83 \times 10^{-10}$ m is the Burgers vector of either a single $1/2\langle 110\rangle$ or a dissociated $1/2\langle 101\rangle$ superdislocation.

A. Deformed microstructures

The main feature observed in the deformed microstructures of this alloy was the extensive twinning activity which was already observed after only 0.8% strain in the specimens crept at the lower stress of 260 MPa. As seen in Fig. 4 some grains were already deformed by several twin systems, as analyzed in the example shown. Detailed diffraction analysis of these twins and others observed under different conditions of strain or applied stress confirmed that they all exhibited the true twin relationship between the matrix and the twinned layer. In this sense the twinned interfaces were exactly the same as the γ/γ interfaces of the true-twin type producing a rotation of 180° around a $\langle 111\rangle$ pole and analyzed in some of our previous work.[18,19] This twinned microstructure was confirmed to be produced by emission and glide of $1/6\langle 112\rangle$ dislocations on {111} planes confirming our previous studies[18,19] and those by other authors.[20]

On the other hand, a large number of grains deform both by mechanical twinning and glide of single dislocations and their density was rather high even after strains as low as 0.8%. This is the case of the example shown in Fig. 5 (using two diffraction conditions) from the specimen crept under 340 MPa. The tensile axis of this grain was near [010] (15° away) and we note that all the dislocations active in the entire grain are invisible with $g = 002$; therefore they are $1/2\langle 110\rangle$ segments. At this higher stress, detailed analysis of the line directions was carried out from grains containing a lower dislocation density such as the one illustrated in Fig. 6. In this grain the tensile axis was close to [110], and besides the twin we see long dislocation segments with Burgers vector $1/2[110]$ (visible with $g = \bar{1}11$ and 111) which have screw character, confirming that the short edge segments propagate by trailing the long screw segments behind. In all cases the long screw segments exhibit pinning points along their lines, with debris and small dislocation loops also detected.

However, many other grains did not deform by mechanical twinning and, although much effort was denoted to investigate a large number of grains in search for other modes of deformation involving superdislocations, only single $1/2\langle 110\rangle$ dislocations were observed in all the grains. Figure 7 shows another example of a grain also deformed to 0.8% strain under 260 MPa which did not deform by twinning, and where only $1/2\langle 110\rangle$ dislocations were active. In this figure we see a grain whose tensile axis was [011], and the images taken under different diffraction conditions confirm the presence of both systems, namely $1/2[110]$ (visible with $g = \bar{1}11$) and $1/2[\bar{1}10]$ (visible with $g = 220$). In both cases the directions of the long segments have been analyzed as the corresponding screw directions while the short segments have pure edge orientation. Thus, the two line directions of each dislocation define the (001) plane on which both types of $1/2\langle 110\rangle$ dislocations propagate trailing the long screw segments behind. The Schmid factor for these slip systems is $m = 0.35$. Also seen in these micrographs are large, elongated loops with the

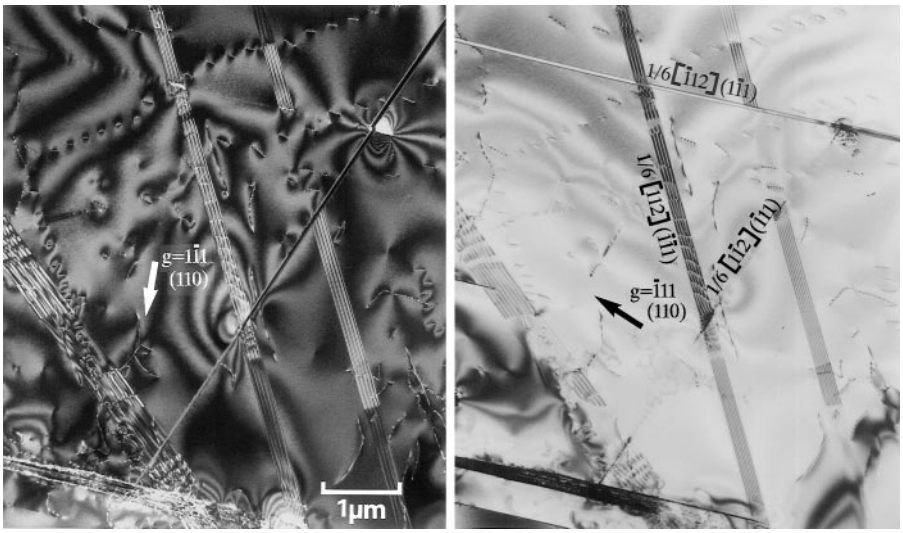

FIG. 4. Example of multiple twinning observed after 0.8% creep strain under 260 MPa.

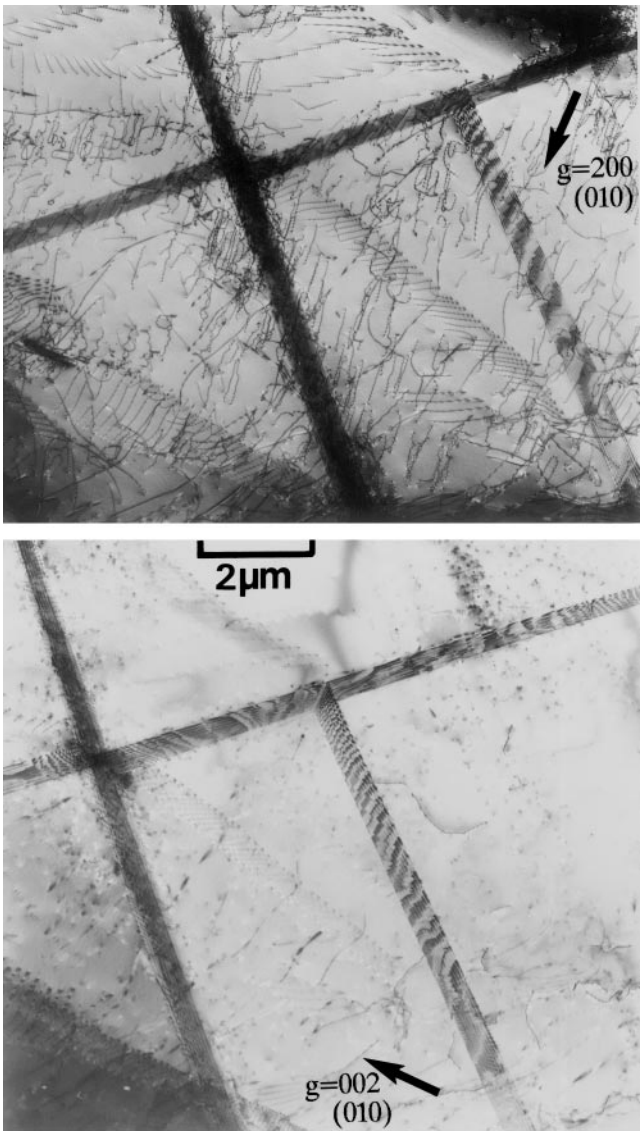

FIG. 5. Typical deformed microstructure observed after 0.8% creep strain under 340 MPa. The tensile axis of this grain is close to [010] (see text for details).

same $1/2\langle 110\rangle$ Burgers vector and also lying on the (001) plane.

After higher creep strains, the major differences observed were the higher density of dislocations and mechanical twins active within given grains. Figure 8 shows an example of a grain observed after 1.5% strain crept under 340 MPa. Here the tensile axis was close to [110] (about 10°) and two twin systems are active together with a high dislocation density. Practically all the dislocations are invisible with $g = 002$ determining their Burgers vector as $1/2\langle 110\rangle$. In the image taken with $g = \bar{1}11$ we note that only a small fraction remain visible, and these have a Burgers vector $1/2[110]$. This means that the large majority of the dislocations observed with $g = 111$ belong to the primary slip system

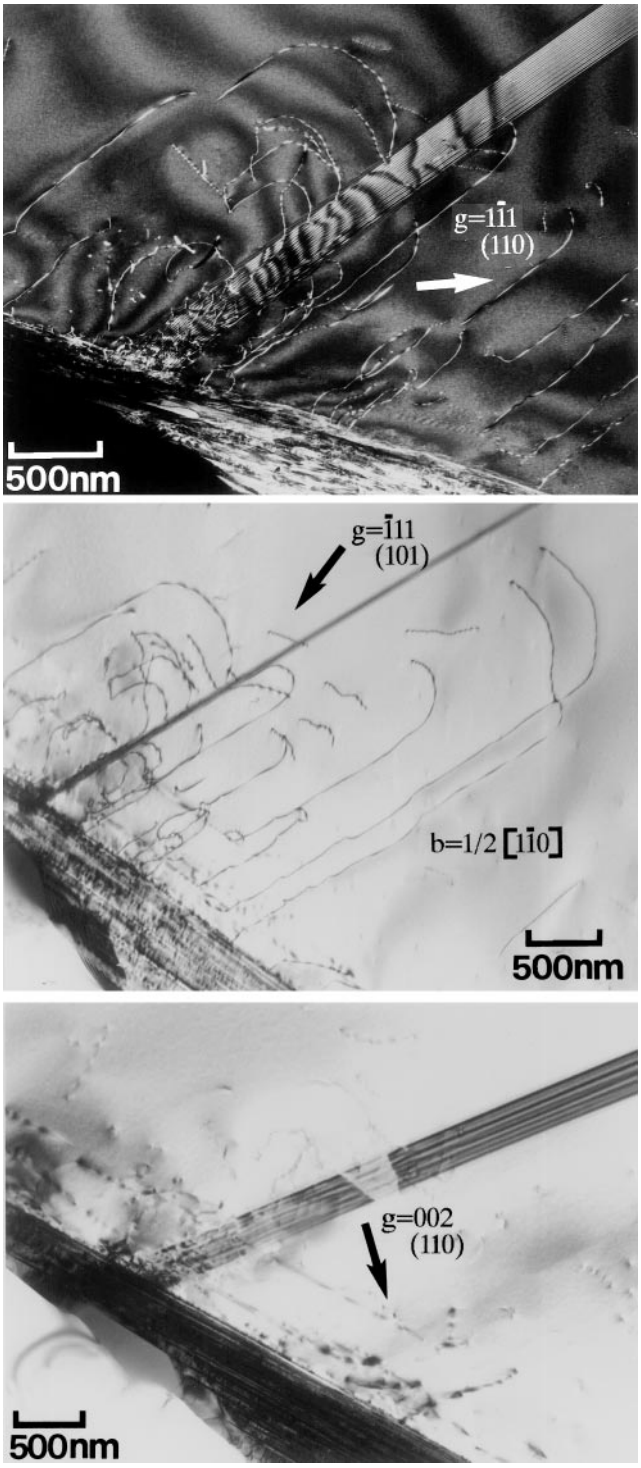

FIG. 6. Typical microstructure observed after 0.8% creep strain under 340 MPa from which Burgers vectors and line directions have been analyzed (see text for details).

and have a Burgers vector $1/2[1\bar{1}0]$. The trace analysis has confirmed that the line direction between pinning points of the bowed segments is $[1\bar{1}0]$; therefore, it is the screw segments that are pinned along their lines.

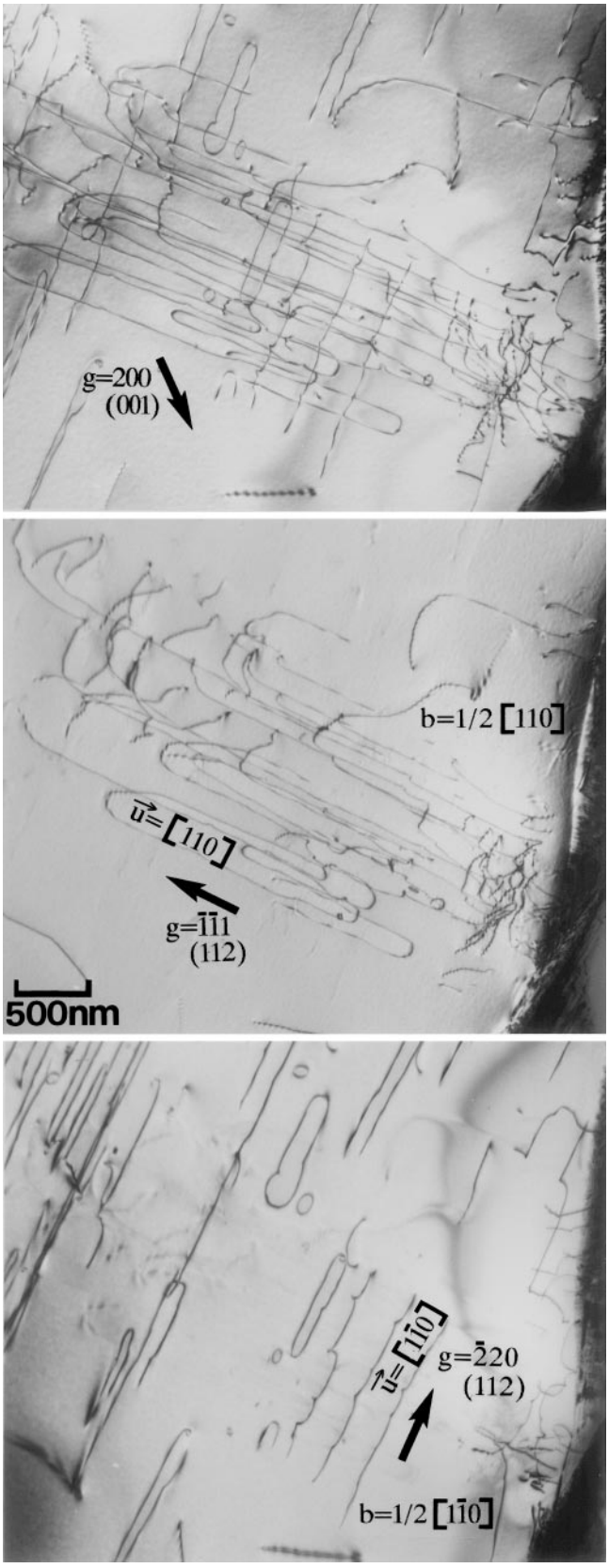

FIG. 7. Typical example of a grain with a tensile axis [001] and deformed by $1/2\langle 110\rangle$ slip (see text for details). Creep conditions $\sigma = 260$ MPa, $\epsilon = 0.8\%$.

Two major twin systems have been analyzed, namely $1/6[112](111)$ and $1/6[112](\bar{1}11)$ both of which have Schmid factors $m = 0.48$ for the specific grain orientation. Figure 9 shows another grain observed after the same creep conditions (namely 1.5% strain under 340 MPa) in which an increase in twinning activity is confirmed compared with samples deformed to lower strains. The tensile axis for this grain is [121] and the major twins subdividing the grains correspond to the system $1/6[112](\bar{1}11)$ which has a Schmid factor $m = 0.47$ for this grain orientation. Also seen are dislocations analyzed as $1/2[110](001)$ with a Schmid factor $m = 0.23$. From this creep condition we show in Fig. 10 detailed images taken by weak beam contrast at two different orientations to allow analysis of the twins and measurement of the twinned layer thickness. The latter was carried out by measuring the spacing between interfaces when the twins are imaged vertically in the foil [as seen in Fig. 10(b)]. The values measured were 20–30 nm and 40–50 nm after respective strains of 0.8 and 2.6% for a stress of 260 MPa (as in Fig. 4) and became about 100 nm after 2.6% strain under 360 MPa.

Figure 11 shows an example of the microstructure observed in specimens crept to a strain after the onset of the minimum creep rate. In this case after 2.6% creep strain we see two adjacent grains that are subdivided by the twin interfaces an also containing a high dislocation density. The latter had a Burgers vector $1/2[110]$ and corresponds to the large majority of the total density, with the second system $1/2[\bar{1}10]$, invisible with this diffraction condition, being a minority number. Since the tensile axis of the large grain is [112], the slip system $1/2[110](001)$ has a Schmid factor $m = 0.47$ while the secondary system cannot glide on plane (001) since the Schmid factor is zero. Thus, at this stage when the minimum creep rate has been reached, the deformation process is characterized by the propagation of single dislocations across the γ matrix between twin interfaces (the twin interfaces being new sites where dislocations accumulate) at the same time as the passage of Schockley partials continues to increase the thickness of the existing twinned layers.

Similar TEM observations made from specimens deformed under constant strain rate conditions confirmed that the same dislocation and mechanical twinning mechanisms were active within the γ grains. Those in which twinning was not active deformed only by single $1/2\langle 110\rangle$ dislocations whose long screw segments were pinned along their length. Also, the emission of $1/2\langle 110\rangle$ edge segments was observed from twin interfaces and grain boundaries. An example of such mechanism is shown in Fig. 12 from a specimen deformed to 2% at a constant strain rate of 4×10^{-6} s^{-1}. The tensile axis of the grain shown is [112] and all the visible dislocations have Burgers vector $1/2[110]$ since they are

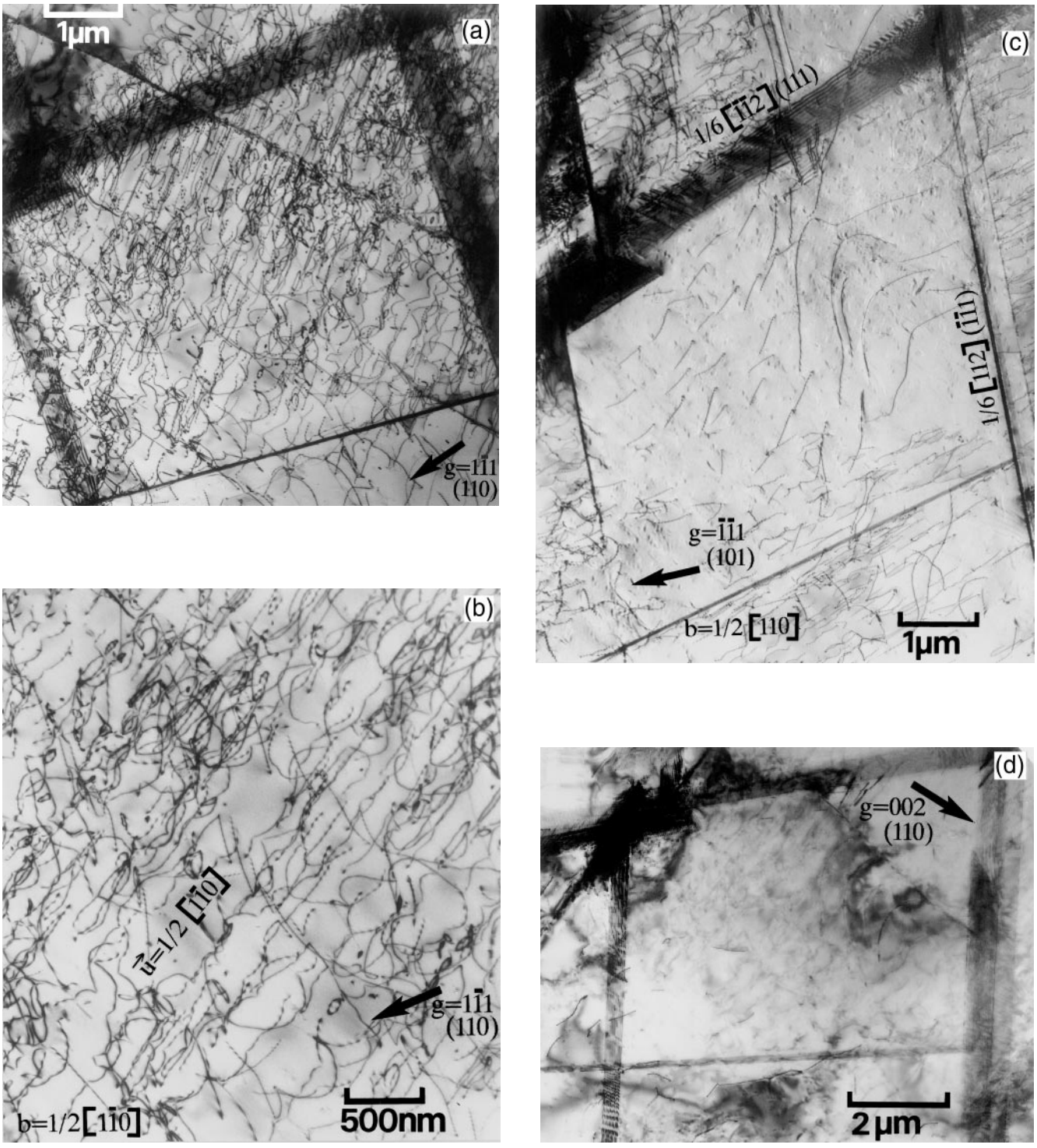

FIG. 8. Deformed microstructure observed after 1.5% creep strain under 340 MPa from a grain with a tensile axis close to [110]. Note in (b) a detail taken from (a) where the $1/2[1\bar{1}0]$ dislocation segments are pinned along their screw orientation and bow out under the action of the local stress.

all invisible with both $g = 002$ and $g = 1\bar{1}1$. Therefore, all the deformation in this grain is produced by a primary slip system. The bowed dislocation segments that are emitted from the grain boundary (see in the lower part of Fig. 12) have pure edge orientation and define the (001) glide plane. For this grain orientation, the Schmid factor of the active slip system $1/2[110](001)$ is $m = 0.47$ while it is zero for a secondary system $1/2[1\bar{1}0](001)$.

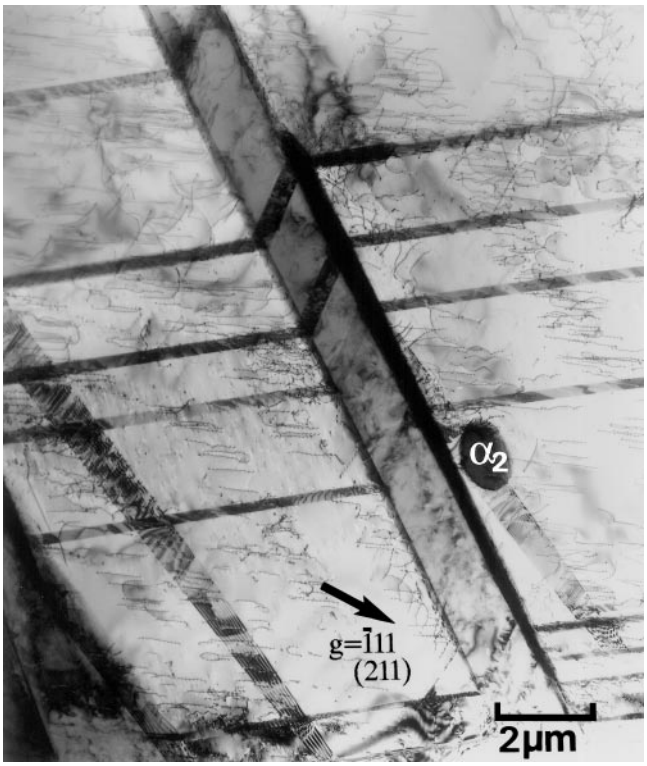

FIG. 9. Deformed microstructure observed after 1.5% creep strain under 340 MPa from a grain with a tensile axis [121] (see text for details).

Although the TEM observations allow correct identification of active deformation mechanisms, the number of deformed γ grains that can be examined is limited. To quantify the total number of grains that deform by mechanical twinning we have examined in the SEM complete deformed sections cut from the gauge length of the specimens perpendicular to the tensile axis. Before examining these disks they were electropolished such that the observation of twins was possible from crystallographic contrast (using backscattered electrons) due to the fact that the thin twinned regions are rotated by 180° with respect to the matrix. Therefore, a thin slab of twinned region appears as a line due to its different crystallographic contrast. Figures 13–15 show examples comparing grains taken from sections of the undeformed specimens (head of tensile sample) and after creep or tensile deformation to different strains. The major difference between the grains of undeformed and deformed samples is the total absence of mechanical twins in the former while in the latter the appearance of mechanical twins is similar to that observed by TEM under the same creep conditions. From these SEM observations a large number of images was accumulated, the total number of twinned grains counted, and the average spacing between twins measured as a function of strain for different conditions of applied stress (at least 300 grains were counted in each case). Figure 16 shows the fraction of twinned grains as a function of strain measured from the crept specimens, and in Table II we see those measured from the specimens tested in tension under a constant strain rate of 4×10^{-6} s^{-1}.

From these values we note that the number of grains that deform by mechanical twinning increases with increasing strain both under creep conditions (constant applied stress) and under constant strain rate tests. Under creep conditions, for a given amount of strain the applied stress seems to have little effect on the number of grains that deform by mechanical twinning, it affects, however, the twinning intensity (total number of twins as well as the thickness of the twinned layer) activated within each grain. This is confirmed by comparing the images in Fig. 14 illustrating twinned grains observed after 2.6% strain under two different stresses of 260 [14(a)] and 340 MPa [14(b)]. The average spacings between twins measured were 5–8 μm and 2–3 μm from the low and high stress, respectively. Similarly, as seen in Fig. 15, in the specimens deformed under constant strain rate conditions not only the total number or twinned grains increases with increasing strain but also the twinning intensity within each grain increases substantially. On the other hand, the fraction of twinned grains reaches a saturation value of about 50% at 6% strain which corresponds to the maximum tensile ductility measured under constant strain rate conditions.

IV. DISCUSSION

The behavior of the alloy under creep will be discussed from the microstructural point of view, taking into account the two stages observed in the creep curves. During the primary stage we measure very high instantaneous strain rates on loading which decrease very fast during the first 1% strain to reach minimum values at about 1.5–2%. Parallel constant strain rate tests have confirmed that work hardening is very pronounced at the onset of plastic flow, decreasing rapidly to about one third of the initial value after 1.5% strain (see Fig. 3). During this period the twinning activity is very pronounced as well as primary slip by $1/2\langle 110\rangle$ dislocations. Since only about 40% of the grains deform by mechanical twinning at the onset of the minimum creep rate, hardening (responsible for the fast decrease of strain rate) is produced by twins in some grains but must

TABLE II. Volume fraction of twinned grains measured from specimens deformed at constant strain rate 4×10^{-6} s^{-1}.

$\epsilon_{plastic}$ (%)	Fv twinned grains (%)
1	34
3	45
6	53

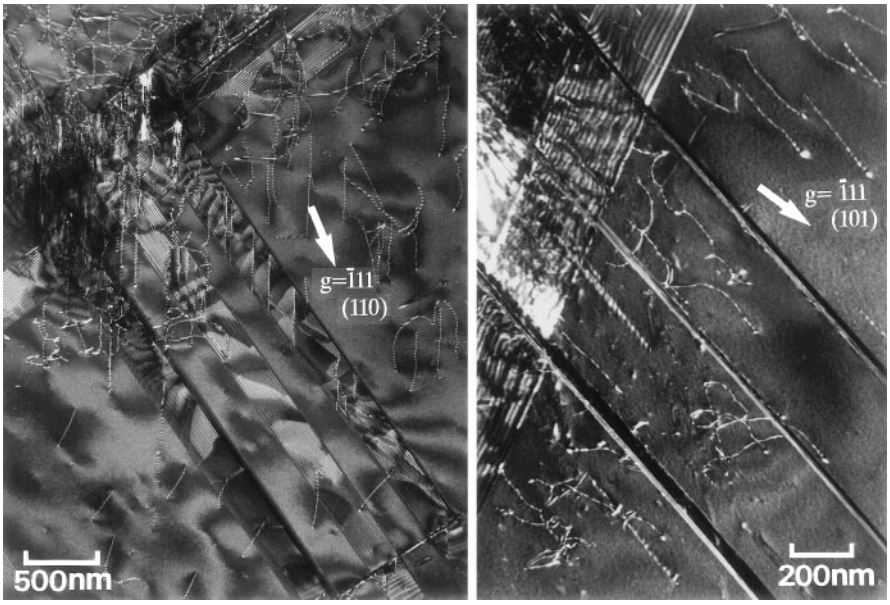

FIG. 10. (a, b) Detailed weak beam images of mechanical twins taken under two different orientations from a deformed grain with tensile axis [110] (σ = 340 MPa, ϵ = 1.5%).

be produced by interactions of $1/2\langle 110\rangle$ dislocations in the rest of the grains.

From the x-ray diffraction as well as from the TEM analysis, we have confirmed that there is no specific texture or preferred grain orientations in this alloy and that the observed twinning activity corresponds to those slip systems favored by the Schmid factors in most cases. In particular, we have noted that grains with tensile orientation [110] exhibit a high twin density of the two systems with maximum Schmid factors (m = 0.48) (as the example in Fig. 8). This is also the case for grains with [001] orientation. On the other hand, grains with tensile axis [121] for which only one twinning system has the maximum Schmid factor m = 0.47 are subdivided by one major twinning system (see Fig. 9). In the case of grains with tensile axis [011] in which the Schmid factor for twinning (m = 0.28) is always lower than that for $1/2\langle 110\rangle(001)$ slip (m = 0.36), the grains deform only by the latter (example of Fig. 7). This is also the case for grains with [112] orientation in which the Schmid factor for $1/2[110](001)$ slip (m = 0.47) is higher than that for twinning (m = 0.32) and the grain is deformed by the former. Thus, twinning is only favored for those twinning systems whose Schmid factors are higher than those to activate single dislocations. The presence of $1/2\langle 110\rangle(001)$ dislocations in grains with a tensile axis near to [010] or [100] (as the example of Fig. 5 with an orientation about 15° from [010]) has been attributed to the local stresses at twin intersections from which emission of these segments has been confirmed in this and other studies.[17–19] In conclusion, the twinning activity observed from the early stages of the creep process is due to the macroscopic applied stress which favors mechanical twinning as a major slip system. Only in the specific grain orientations for which $1/2\langle 110\rangle(001)$ slip has a larger Schmid factor than twinning does slip take over. This does not exclude the activation of twinning in that type of grain due to hardening at a later stage in the deformation process when local constraints across adjacent grains will determine local shear stresses responsible for the deformation process.

The contribution that twinning dislocations make to the total strain of the material has been estimated for the two extreme values of stress used, for which measurements of the twin spacings and of the twinned layer thickness have been made. From the microstructure obtained after 1.5% strain at 360 MPa, the spacing between twins in the matrix, d_{twin}, was measured as about 2 μm, and the twinned layer thickness, t_{twin} as 80 nm. Assuming that all the twins traverse the grains of diameter D = 12 μm, and section area, $S = 1.13 \times 10^{-10}$ m^2, the number of twins per grain is given by $N_t = D/d_{\text{twin}} = 6$ and the twin density (number of twins/area) is $N_t/S = 5.3 \times 10^{10}$ m^{-2}. Since twin propagation occurs by glide of $1/6\langle 112\rangle$ dislocations on every adjacent {111} plane,[20] the number of twin dislocations can be obtained by dividing the twinned layer thickness by the interplanar spacing of {111} planes (d_{111} = 0.2316 nm). Thus, for an average layer thickness of 80 nm we obtain value of about 345 dislocations per

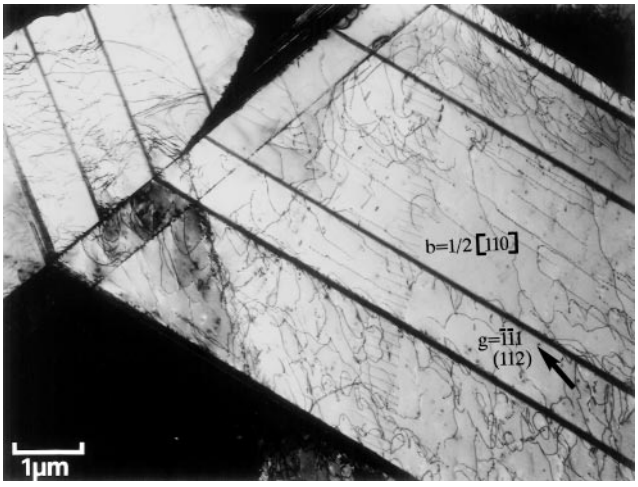

FIG. 11. Deformed microstructure observed at the onset of minimum creep rate from a grain with tensile axis [112] (σ = 340 MPa, ϵ = 2.6%).

twin. Multiplying this number by the twin density we calculate a twinning dislocation density, $\rho_{twin} = 1.8 \times 10^{13}$ m^{-2}. Since these dislocations traverse the entire grains, the total shear strain produced by this twinning process is $\gamma_{twin} = \rho_{twin} bD$, where b is the Burgers vector of the twinning dislocation $\approx 1.6 \times 10^{-10}$ m and D the grain size. This yields a contribution to the total creep strain by twin activity $\gamma_{twin} = 0.036$. This value corresponds to a macroscopic strain $\epsilon_{twin} = \gamma_{twin}/3 = 0.012$. Since the total fraction of grains that deform by mechanical twinning is only 40%, this corresponds to a total contribution to the creep strain $\epsilon_{twin} = 0.0048$ (≈0.5%), which is about 30% of the total strain of the specimens studied. Similar calculations made from the specimen crept at the lower stress of 260 MPa, where the matrix spacing between twins was measured as about $d_{twin} = 6$ μm and the twinned layer thickness, $t_{twin} = 40$ nm, yield a total contribution of the twin activity to the macroscopic strain, $\epsilon_{twin} = 0.001$ (≈0.1%), which is only 7% of the total creep strain produced in the specimen. It is interesting to note that the contribution from twinning to the total creep strain increases with increasing applied stress.

Therefore, the importance of the twins is not so much that they are responsible for a significant amount of strain, but that they lead to a subdivision of the microstructure during the primary stage of creep reducing the mean free path of the $1/2\langle 110\rangle$ dislocations as they propagate between twins instead of propagating across the entire grain. As the dislocations are accumulated at twin interfaces, this leads to a decrease of strain rate. However, in those grains that do not deform by mechanical twinning the same decrease in strain rate needs to occur to ensure a homogeneous deformation of the specimen, and this can occur either by a decrease

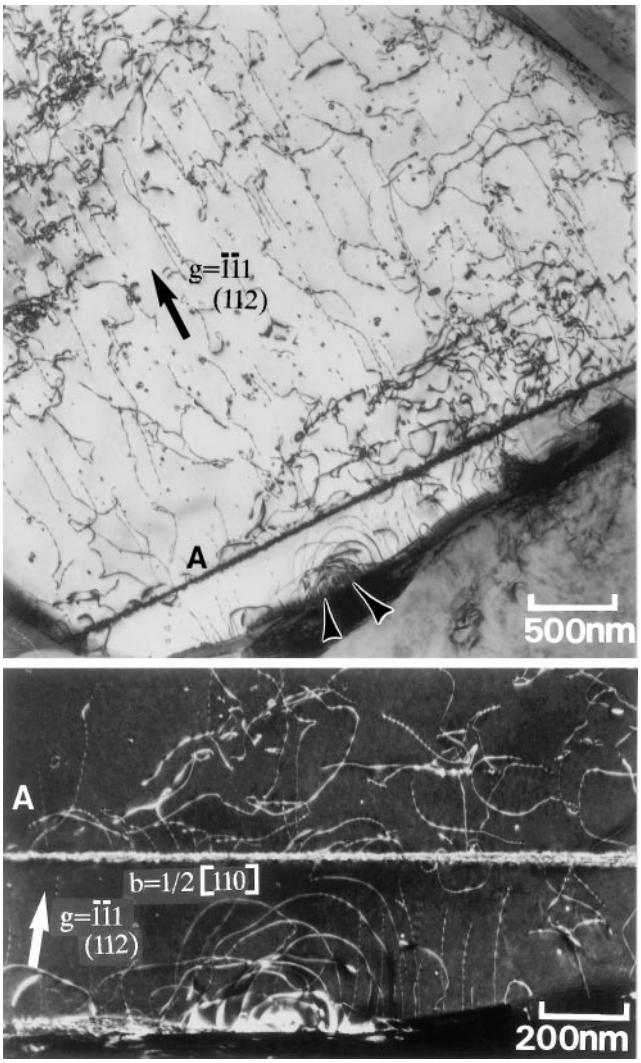

FIG. 12. Example of deformed microstructure observed after tensile deformation at constant strain rate 4×10^{-6} s^{-1}, ϵ = 2%. Note the bowed segments being emitted from the boundary (marked by the arrows).

in the density of primary $1/2\langle 110\rangle$ dislocations or by a decrease of their speed. In this way, the twinning activity determines (directly or indirectly) the hardening process observed during the primary stage of creep.

Thus, at the end of the primary stage the minimum creep rate is reached by the exhaustion of mobile $1/2\langle 110\rangle$ dislocations, either because they accumulate at twin interfaces or grain boundaries or because their high density leads to a large number of pinning points and debris within the γ matrix. Since we have observed that in a large number of grains the majority of dislocations correspond to a primary slip system only (see Figs. 8 and 12), the existence of large numbers of pinning points cannot be attributed to a forest cutting mechanism. Instead the pinning events seen along the screw segments are produced by intrinsic obstacles that exist in the γ

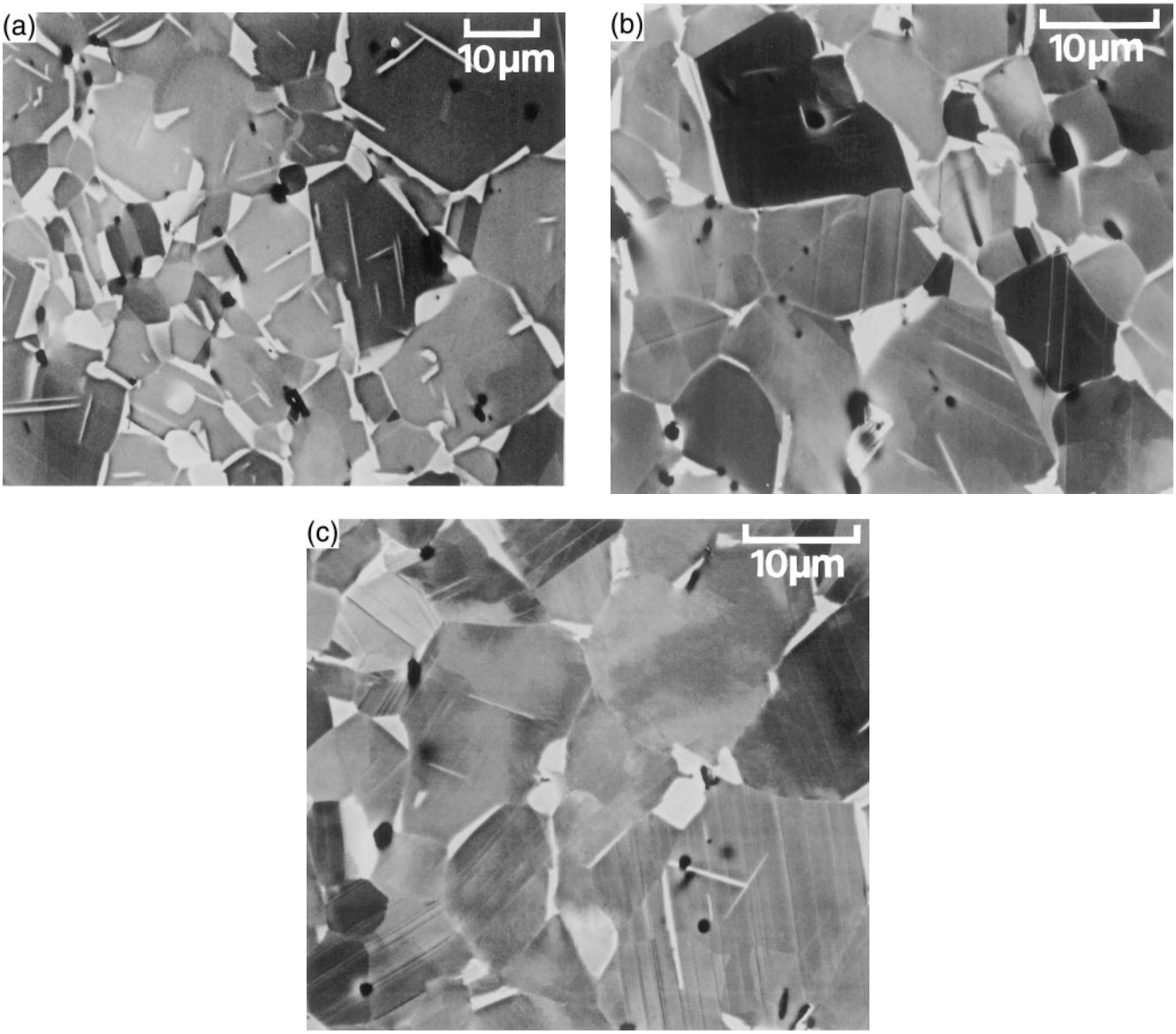

FIG. 13. Examples of microstructures observed by crystallographic contrast in the SEM. Note the absence of mechanical twins in the undeformed sample (a) and the existence of twinned grains after creep conditions (b) $\sigma = 260$ MPa, $\epsilon = 1.5\%$ and (c) $\sigma = 340$ MPa, $\epsilon = 2.6\%$.

matrix and that hinder dislocation motion. This leads to intrinsic hardening as observed in the early stages of deformation during tensile tests performed under constant strain rate (see Fig. 3) or during the primary stage of creep. These conclusions are confirmed by the strain-independent values of activation volumes measured during the strain rate jump tests and also by TEM observations that show that the number of cusps seen along the $1/2\langle 110\rangle$ segments does not change significantly with strain. A strain-rate controlling mechanism that is independent of strain eliminates forest cutting as a possible mechanism since the latter would imply a decreasing value of activation volume with increasing dislocation density and, thus, with increasing strain.[21]

Instead, two mechanisms can be proposed as controlling deformation: lattice friction or solute pinning. When lattice friction controls the dislocation mobility, we expect smaller values of the activation volumes (i.e., $10–50b^3$). However, the higher values obtained in our study might represent a deformation process controlled by solute atoms (or fine particles) pinning the dislocations at certain intervals, L dependent on solute concentration, c, $L = bc^{-1/2}$. Then the activation volumes would be determined by the solute concentration as $V = c^{-1/2}\, b^3$. The activation volume measured experimentally ($330b^3$) would correspond to very small solute concentrations (of the order of 10 ppm) which does not fit with Nb or Cr being the solute atoms responsible for the pinning effect.

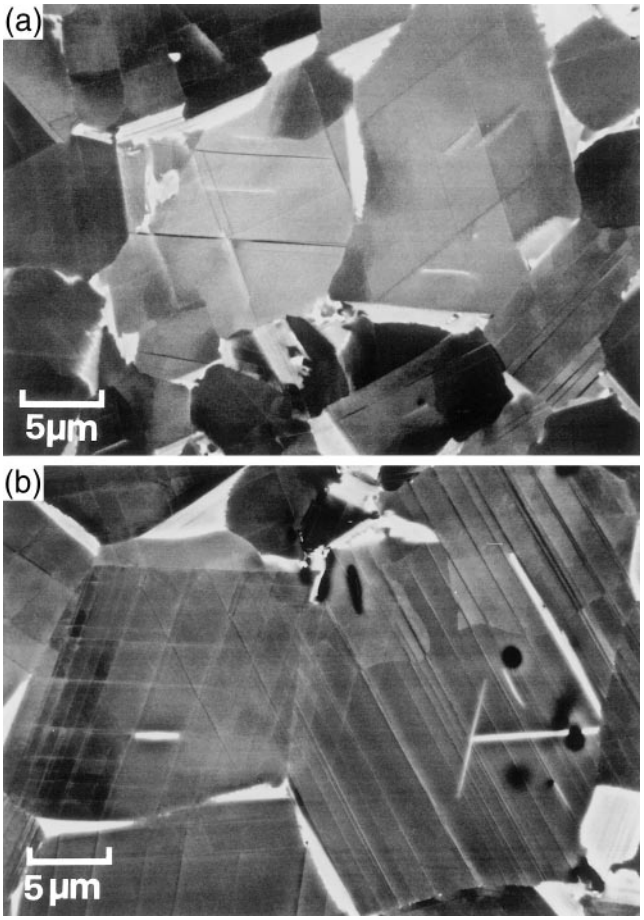

FIG. 14. Comparison of the different twinning intensity (twin thickness and separation between twinned layers) observed after 2.6% creep strain under two different stresses: (a) 260 MPa and (b) 340 MPa.

Other impurities (such as oxygen, boron, or even carbon) could produce this effect.

During the secondary stage of creep (i.e., between 2 and 3% strain) the strain rate remains rather constant near its lower value. During this stage our observations confirm that the deformation process is characterized by dislocation motion across twin interfaces or across entire γ grains (depending on whether the grains have been subdivided by mechanical twinning or not). In order to analyze the thermally activated mechanism that controls the constant strain rate we have examined the details of dislocation configurations to determine whether the observed motion of $1/2\langle 110\rangle$ dislocations on (001) planes involved climb processes. Figure 17 shows a detailed example of $1/2\langle 110\rangle$ dislocation segments and loops together with a schematic diagram which shows the glide and climb planes that could possibly be involved. The $1/2[110]$ segments and loops shown are characterized by the two major line directions [110] (screw orientation) and [1$\bar{1}$0] (pure edge) and lie on the (001) plane. If climb processes were involved this should take place on the (110) plane shown, perpendicular to the Burgers vector, and this would mean that there should be a pure edge segment trailing behind. Instead we observe that the loops are on (001) planes and that the trailing segments left behind have screw orientation. This confirms that the $1/2\langle 110\rangle$ dislocations observed in our alloy propagate on (001) planes by glide only and climbing processes are not involved.

From the values of minimum creep rates we have evaluated the stress exponent, n, characterizing the dependence on applied stress given by the general power law equation: $\dot{\epsilon} = \sigma^n \exp -(Q/RT)$. Figure 18 shows the plot $\ln \dot{\epsilon}$ versus $\ln \sigma$ from which the stress exponent was obtained as the slope of the line. The values obtained, $n = 8$, is typical of this type of alloy[11,14] and indicates that the secondary stage of creep cannot be described by simple recovery processes.[22] When such high stress exponents are obtained, it is possible to rationalize the creep behavior assuming the existence of an athermal threshold stress, σ_0, and express the strain rate as: $\dot{\epsilon} = A\ (\sigma - \sigma_0)^{n'} \exp(-Q/RT)$. This threshold stress represents a friction stress or a stress concentration that needs to be overcome to initiate dislocation mobility in the γ matrix. As a consequence the thermally activated glide of dislocations takes place under the action of the effective stress represented by the term $\sigma - \sigma_0$. To obtain the value of the threshold stress, the stress exponent n' used should be that normally obtained for creep of the matrix in the absence of other obstacles. Generally, in pure metals this value ranges between $n' = 3$ and 5 and in the case of single phase TiAl alloys deformed at low stresses the value obtained is $n' = 4$.[6] Using this value we have plotted in Fig. 19 the applied stress, σ, versus $\dot{\epsilon}^{1/4}$ and from the intercept of the line obtained we have measured the threshold stress as $\sigma_0 = 167$ MPa. On the other hand, the threshold stress varies with the value n' such that for $n' = 3$ we obtain $\sigma_0 = 130$ MPa and for $n' = 5$ we have $\sigma_0 = 202$ MPa. Under such conditions it is difficult to justify the threshold stress concept, and for this reason, when high stress exponents are observed and thermally activated glide of dislocations has been confirmed, it is more appropriate to interpret the creep data using an equation in which the creep rate is expressed as[23]:

$$\dot{\epsilon} = \dot{\epsilon}_0 \exp -\left(\frac{Q_0 - V\tau_{\mathrm{loc}}}{RT}\right),$$

where $\dot{\epsilon}_0$ represents a temperature independent parameter that will depend on the microstructure. The term inside the exponential corresponds to an apparent activation energy, $Q = Q_0 - V\tau_{\mathrm{loc}}$ which can be considered as the sum of two terms: the thermal energy itself, Q_0, and a mechanically produced energy, $V\tau_{\mathrm{loc}}$. The term V is known as the activation volume, better expressed as the

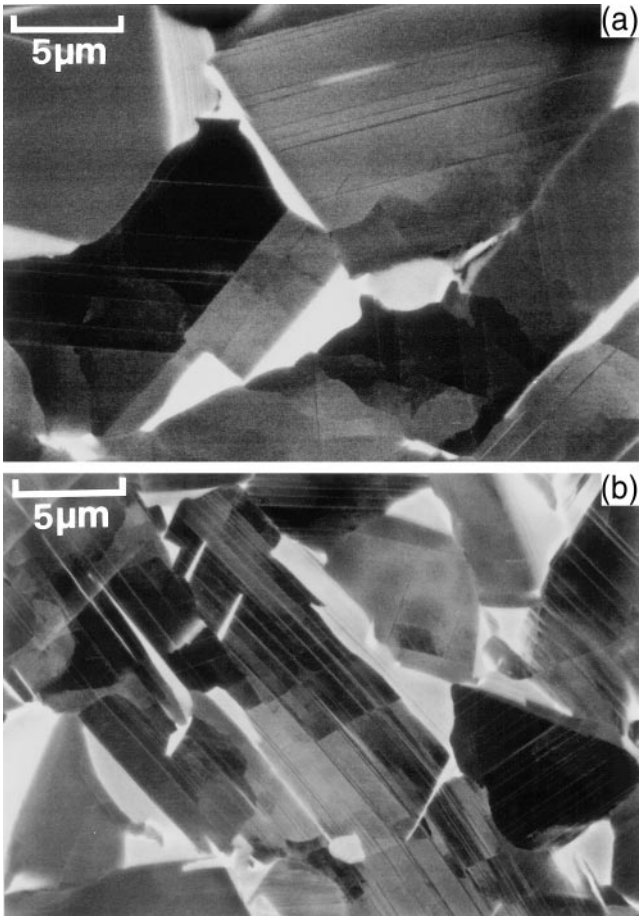

FIG. 15. Increased twinning intensity with increasing strain observed after tensile deformation at constant strain rate 4×10^{-6} s^{-1}. (a) $\epsilon = 1\%$ and (b) $\epsilon = 3\%$.

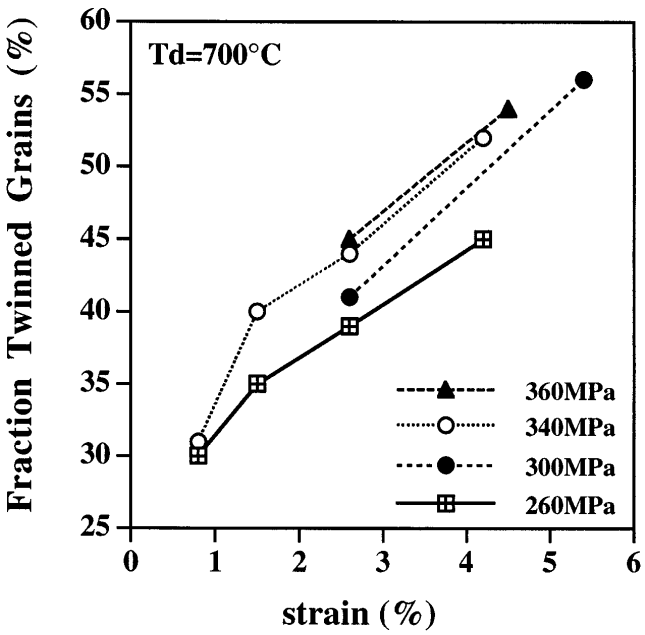

FIG. 16. Plot of the fraction of grains deformed by mechanical twinning as a function of strain measured from the specimens crept under different applied stresses.

product $V = Ab$, of the activation area A over which the activated event occurs and the Burgers vector. The value τ_{loc} is the local shear stress acting on the dislocation segment helping the thermally activated event to occur.

In our alloy we have measured a high value of activation energy, $Q = 430$ kJ/mol, much higher than that for self-diffusion ($Q_{self\text{-}dif} \approx 300$ kJ/mol), indicating that the value measured represents an apparent activation energy. Introducing this value in the above equation as well as that of our experimentally measured activation volume, V, we have been able to calculate the value of the local shear stress, τ_{loc}, acting on the thermally activated dislocation segment. Two possible cases need to be considered, one in which a self-diffusion process is taking place (i.e., $Q_0 \approx 300$ kJ/mol) that results in a value of the local shear stress $\tau_{loc} = 30$ MPa. The second case assumes a thermally activated mechanism controlled by a process such as pipe diffusion or cross-slip (i.e., $Q_0 \approx 150$kJ/mol) and leads to a local shear stress $\tau_{loc} = 62$ MPa. This latter value represents the shear stress necessary to bow out a dislocation segments of size $L = 250$–300 nm ($\tau = \mu b/L$) and is consistent with the link length of $1/2\langle 110\rangle$ segments typically seen between pinning points in our micrographs [see Fig. 8(b)]. Thus we would like to suggest that this local stress represents the athermal stress necessary to bow out a dislocation segment and unpin it over a given length to initiate its movement in the γ matrix. According to the analysis made here, we suggest that the activation energy required to allow thermally activated glide of dislocations is that corresponding to pipe diffusion along the dislocation core or cross-slip, which must be required for segments to break away from their pinning points.

V. CONCLUSIONS

The creep behavior of a γ-based TiAl alloy with equiaxed microstructure and fine grain size has been analyzed using detailed observations of the deformation process as a function of strain and applied stress.

One important feature of the creep process is the extensive twinning activity observed from the early stages of deformation. Although the total fraction of grains that twin increases with increasing strain it tends to saturate at about 50%. Also, for a given amount of strain the applied stress seems to have little effect on the number of grains that deform by mechanical twinning, but affects, however, the twinning intensity activated within each grain.

However, the importance of the twins is not their contribution to the total amount of strain, but that they

lead to a subdivision of the microstructure during the primary stage of creep reducing the mean free path of the $1/2\langle 110\rangle$ dislocations and leading to a decrease in strain rate. In those grains that do not twin, the decrease in strain rate occurs either by a decrease in the density of primary $1/2\langle 110\rangle$ dislocations or by a decrease of their speed. In this way, the twinning activity determines (directly or indirectly) the hardening process observed during the primary stage of creep.

We suggest that the mechanism controlling the creep rate during the secondary stage of creep is the thermally activated glide of $1/2\langle 110\rangle$ dislocations which becomes possible as the screw segments can bow out between pinning points under the action of a local athermal stress with the help of processes such as the pipe diffusion energy along the dislocation core or cross-slip.

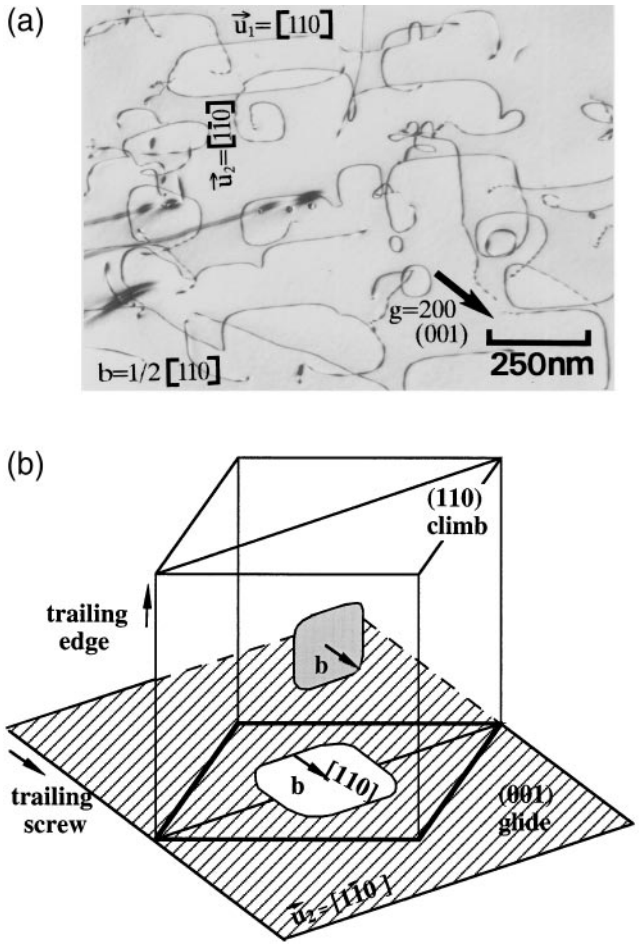

FIG. 17. (a) Detailed example of typical $1/2[110]$ dislocation segments showing analyzed line directions [1$\bar{1}$0] and [110], and (b) schematic diagram confirming that a climb process is not possible since the trailing segments has screw orientation (σ = 260 MPa, ϵ =0.8%).

ACKNOWLEDGMENTS

We would like to thank Professor D. G. Morris for reading this manuscript and for the many useful discussions. F. Maccabiani is also acknowledged for carrying out some of the tensile and creep tests. The

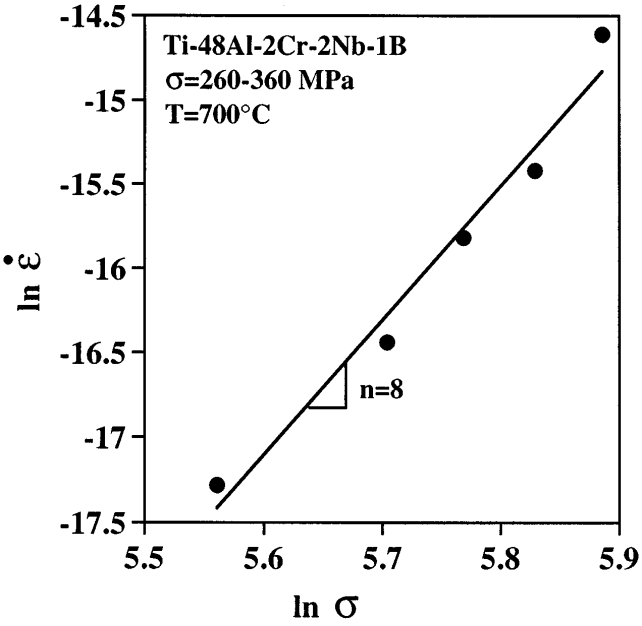

FIG. 18. Plot $\ln \dot{\epsilon}$ versus $\ln \sigma$ from which the stress exponent n = 8 has been obtained.

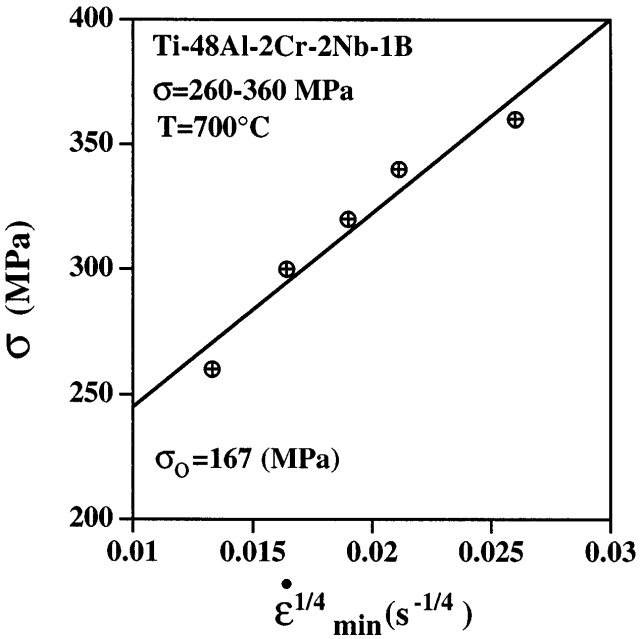

FIG. 19. Plot of the applied stress, σ, versus $\dot{\epsilon}^{1/4}$ from which the threshold stress σ_0 has been measured.

OFES is also acknowledged for financing this study under the project COST 513.

REFERENCES

1. Y. W. Kim and F. H. Froes, *High Temperature Aluminides and Intermetallics*, edited by S. H. Whang, C. T. Liu, D. P. Pope, and J. U. Stiegler (TMS, Warrendale, PA, 1990), p. 465.
2. M. P. Brady, W. J. Brindley, J. L. Smialek, and I. Locci, JOM **48**, 46 (1996).
3. T. Takahashi, H. Nagai, and H. Oikawa, Mat. Trans. JIM **30**, 1044 (1989).
4. R. W. Hayes and B. London, Acta Metall. Mater. **40**, 2167 (1992).
5. M. Es-Souni, A. Bartels, and R. Wagner, Acta Metall. Mater. **43**, 153 (1995).
6. J. Beddoes, W. Wallace, and L. Zhao, Int. Mat. Rev. **40**, 197 (1995).
7. S. Mitao, S. Tsuyama, and K. Minakawa, Mater. Sci. Eng. A **41**, 51 (1991).
8. M. F. Bartholomeusz, Q. Yang, and J A. Wert, Scripta Metall. **29**, 389 (1993).
9. R. W. Hayes and P. A. McQuay, Scripta Metall. Mater. **30**, 259 (1994).
10. B. D. Worth, J. W. Jones, and J. E. Allison, Metall. Mater. Trans. A **26**, 2947 (1995).
11. D. A. Wheeler, B. London, and D. E. Larsen, Jr., Scripta Metall. Mater. **26**, 934 (1995).
12. R. W. Hayes and P. L. Martin, Acta Metall. Mater. **40**, 2761 (1995).
13. J. N. Wang, A. J. Schwartz, T. G. Nieh, C. T. Liu, V. K. Sikka, and D. Clemens, in *Gamma Titanium Alumindes*, edited by Y-W. Kim, R. Wagner, and M. Yamaguchi (TMS, Warrendale, PA, 1995), p. 949.
14. J. Beddoes, L. Zhao, J. Triantafillou, P. Au, and W. Wallace, in *Gamma Titanium Aluminides*, edited by Y-W. Kim, R. Wagner, and M. Yamaguchi (TMS, Warrendale, PA, 1995), p. 959.
15. H. Oikawa, *High Temperature Aluminides and Intermetallics*, edited by S. H. Whang, C. T. Liu, D. P. Pope, and J. U. Stiegler (TMS, Warrendale, PA, 1990), p. 353.
16. Z. Jin, S-W. Cheong, and T. Bieler, in *Gamma Titanium Aluminides*, edited by Y-W. Kim, R. Wagner, and M. Yamaguchi (TMS, Warrendale, PA, 1995), p. 975.
17. M. A. Morris, Intermetallics **5**, 339 (1997).
18. M. A. Morris, Philos. Mag. A **68**, 237 (1993).
19. J. Luster and M. A. Morris, Metall. Mater. Trans. **26A**, 1745 (1995).
20. Z. Jin and T. R. Bieler, Philos. Mag. A **71**, 925 (1995).
21. P. Groh, *Dislocations et Déformation Plastique*, edited by P. Groh, L. P. Kubin, and J. L. Martin (Diffusion les Editions de Physique, Societé Française de Physique, 1979), p. 67.
22. T. G. Langdon, in *Dislocation and Properties of Real Materials* (The Institute of Metals, London, 1985), p. 221.
23. J. P. Poirier, *Plasticité à Haute Temperature des Solides Cristallins* (Editions Eyroles, Paris, 1976).